Direct Coordination of Pterin to Fe^{II} Enables Neurotransmitter Biosynthesis in the Pterin-dependent Hydroxylases

*Shyam R. Iyer,[a] Kasper D. Tidemand,[b] Jeffrey T. Babicz Jr.,[a] Ariel B. Jacobs,[a] Leland B. Gee,[a] Lærke T. Haahr, Yoshitaka Yoda,[c] Masayuki Kurokuzu,[d] Shinji Kitao,[d] Makina Saito,[d] Makoto Seto,[d] Hans E. M. Christensen,[b] Günther H. J. Peters,[b] Edward I. Solomon[a,]**

[a]Department of Chemistry, Stanford University, 333 Campus Drive, Stanford, California, 94305, United States
[b]Department of Chemistry, Technical University of Denmark, Kgs. Lyngby, Denmark
[c]Japan Synchrotron Radiation Research Institute, Hyogo 679-5198, Japan
[d]Institute for Integrated Radiation and Nuclear Science, Kyoto University, Osaka, 590-0494, Japan
[e]Bioneer A/S, 2970 Hørsholm, Denmark

Corresponding Author
*Email: solomone@stanford.edu

Supplementary Information

Materials and Methods

Expression and Purification of the catalytic domain of human Tryptophan Hydroxylase Isoform-2 (chTPH2)

Expression and purification of chTPH2 was done using a previously published procedure except that the buffers did not contain glycerol and were not flushed with argon prior to usage.[1]

Preparation of anaerobic chTPH2 samples for spectroscopic and kinetic studies

Samples for spectroscopy were prepared under an inert atmosphere inside an N_2-purged Vacuum Atmosphere Nexus-1 wet box (<1 ppm oxygen). TPH was made anaerobic by purging under a nitrogen atmosphere on a Schlenk line at 0°C for approximately 1 hour and buffer exchanged inside the inert wet box. The kinetic studies presented were performed in protonated and deuterated 150 mM HEPES, 100 mM $(NH_4)_2SO_4$ and 20 w/v% sucrose buffer (pH/pD 7, buffer A). For the MCD samples, the anaerobic solution in deuterated buffer was saturated with deuterated sucrose to make a frozen glass. Pterin (BH_4) and tryptophan (when required) were added from anaerobic concentrated stock solutions in protonated or deuterated buffer.

Rapid Freeze Quench (RFQ) technique to trap Intermediate

RFQ samples were prepared by mixing anaerobic (Fe^{II}/BH_4/Trp)-TPH with O_2 saturated buffer using a Kintek RFQ-3 system and ejecting the intermediate onto a copper block submerged in liquid nitrogen being spun on a 3" lazy Susan turntable. The frozen intermediate was then powdered on a liquid nitrogen cooled metal block and packed into the sample cell or tube.

Spectroscopic Studies – Magnetic Circular Dichroism (MCD), Mössbauer, Stopped-Flow UV-Vis and resonance Raman

MCD Spectroscopy. The anaerobic Fe^{II}-TPH solutions were saturated with deuterated sucrose and loaded into an MCD cell. Near-IR (600 nm – 2000 nm) MCD spectroscopy was performed using a JASCO J-730 spectropolarimeter equipped with an InSb photodiode detector cooled with liquid nitrogen and fitted with an Oxford Instruments SM4000-7T superconducting magnet. UV-Vis MCD (300 nm – 900 nm) spectroscopy was performed using a JASCO J-810 spectropolarimeter equipped with a photomultiplier tube and fitted with an Oxford Instruments SM4000-7T superconducting magnet. The sample temperature was measured using a calibrated Cernox resistor from Lakeshore Cryotronics. MCD spectra were corrected for zero-field baseline effects by subtracting the corresponding 0 T scan from the data. Variable temperature, variable field (VTVH) MCD isotherms were collected at 8 temperatures between 2 and 25 K and at 12 fields between 0 and 7 T.

Mössbauer Spectroscopy. Mössbauer spectra were collected at 10 K using a See Co. W302 resonant gamma ray spectrometer using a 1.85-GBq ^{57}Co source (Be window, Rh matrix) and with zero external magnetic field. All isomer shifts are given relative to Fe metal at room temperature. Spectra were analyzed and fit using WMoss software package (See Co.) with simulated linewidths (Γ) of 0.4 mm/s.

Stopped-Flow UV-Vis Spectroscopy. Stopped-flow absorption experiments were carried out at 4°C using an Applied Photophysics SX19 stopped-flow spectrophotometer using a 1 cm path length equipped with a photodiode array (300-700 nm) inside a purge glove box in an Ar

atmosphere. The time trace at 248 nm was collected using a photomultiplier tube. O_2-free solutions of (Fe^{II}/BH_4/Trp)-TPH were prepared as described above. The TPH solutions were mixed with an equal volume of buffer that was saturated with O_2 gas at 0°C then allowed to reach equilibrium at 4°C before mixing for 1 mM O_2 experiments. For lower O_2 concentrations, the saturated O_2 solution was diluted with anaerobic buffer, then allowed to reach equilibrium at 4°C before mixing. Kinetic simulations were performed with COPASI.[2]

Resonance Raman Experiments. Resonance Raman spectra were recorded on a Spex 1877 CP triple monochromator with 1,200, 1,800, and 2,400 grooves per millimeter of holographic spectrograph gratings and detected by an ANDOR Newton CCD detector cooled to -80°C. Excitation was provided by a Coherent I90C-K Kr ion laser or an Innova Sabre 25/7 Ar CW ion laser. The spectral resolution is 2 cm^{-1}. rR data were collected as the sample was immersed in a liquid-nitrogen-cooled (77 K) EPR finger Dewar (Wilmad). Laser power was ~20 mW at the sample.

NRVS. ^{57}Fe nuclear resonance vibrational spectroscopy (NRVS) data were collected at the synchrotron light source SPring-8 (BL09XU, C-mode bunch) in Hyōgo, Japan. Samples were mounted on a copper cold-finger cryostat cooled by Helium gas flow to 5-10 K. The NRVS energy scale was calibrated using [NEt_4][$^{57}FeCl_4$] solid powder. Spectral data were processed with spectra.tools which utilizes the PHOENIX program to sum the data and generate the ^{57}Fe partial vibrational density of states.[3,4] True sample temperature was calculated by PHOENIX from the ratio of vibrational annihilation:creation intensity (detailed balance) and ranged from 50 to 70 K. All samples were reproduced 2 times.

Computational Methods

The initial structural model of the (Fe^{II}/BH_4/Trp)-TPH active site was generated from a pterin and alternative substrate bound phenylalanine hydroxylases crystal structure (PDB ID: 1KW0). All subsequent structures were generated by geometry optimization using density functional theory (DFT). These calculations were performed using Gaussian 09[3] with the BP86 functional with 10% Hartree-Fock Exchange in combination with Grimme's empirical correction to dispersion (D3)[4], def2TZVP basis set on Fe and O_2 and def2SVP basis set on the rest of the atoms.[5] The effects of the protein environment were included by using a polarized continuum model (PCM) with a dielectric constant, $\varepsilon = 4.0$.[6] Vibrational frequencies and normal modes and Gibbs free energy changes were obtained using frequency calculations on the optimized structures. Molecular orbital compositions were calculated using QMForge[7] and molecular orbital contours were generated using LUMO[8] and/or IQmol[9]. Time-dependent (TD) DFT calculations were performed using Gaussian 09 to compare with experimental data.

Defining Coordination Geometry Using Magnetic Circular Dichroism (MCD) Spectroscopy

Low-temperature (LT) magnetic circular dichroism (MCD) spectroscopy probes the Fe^{II} $^5T_2 \rightarrow {}^5E$ ligand-field (LF) transition energies and splittings, which define coordination number and geometry.[10,11] A six-coordinate (6C) site has two MCD transitions around 10,000 cm^{-1} split by <2,000 cm^{-1}. A five coordinate (5C) square pyramidal (SP) site has one transition above 10,000 cm^{-1} with the other around 5,000 cm^{-1}, while a 5C trigonal bipyramidal (TBP) site has one transition <10,000 cm^{-1} and the other <5,000 cm^{-1}. From the MCD data in Fig. 1A (*bottom, inset*), in going from the pterin bound Fe^{II}-TPH complex (blue) to the pterin and tryptophan bound ternary Fe^{II}-TPH complex (red), a low energy feature appears (~5,600 cm^{-1}) that defines a 5-coordinate site primed for O_2 reactivity. In the MCD spectrum for the ternary complex, there are three observed transitions in the near-infrared energy region at 5490, 8400 and 9630 cm^{-1}. The presence of three bands reflects a mixture of two distinct iron sites, as a single Fe^{II} site can only have two ligand field transitions in this spectral region.[10] This mixture of Fe^{II} sites is confirmed by Mössbauer spectroscopy, as there are two Fe^{II} quadrupole doublets present in the experimental data (Fig. 3A) and quantifies the amount of each.

MCD Temperature Dependence of the 330nm (30,000 cm^{-1}) Absorption Feature

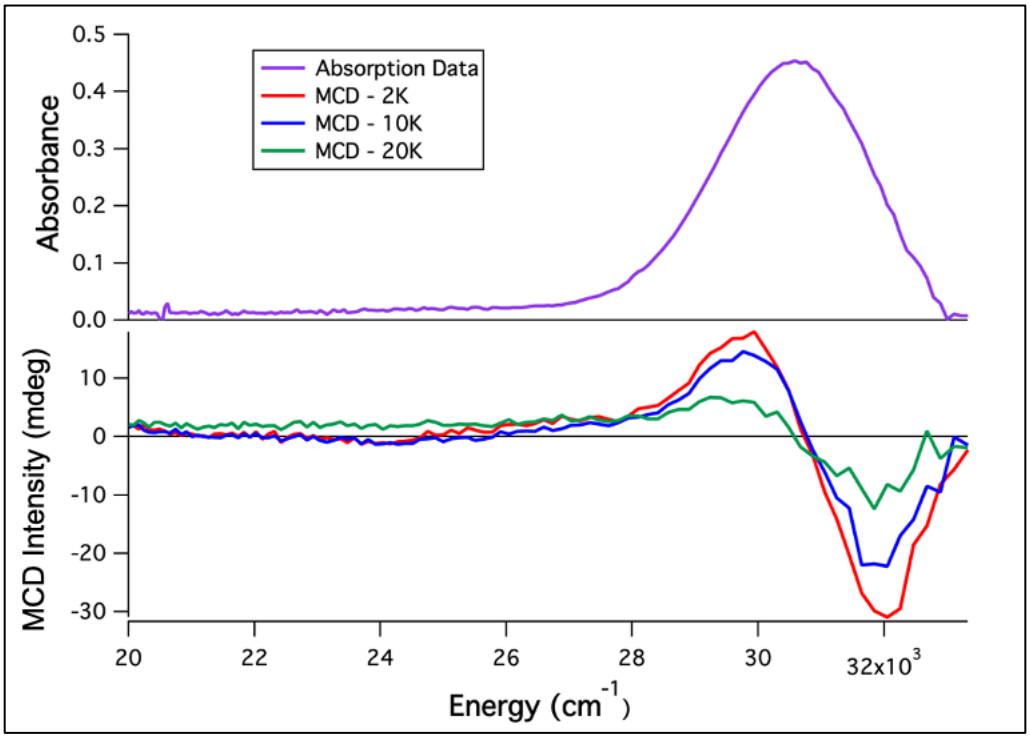

Fig. S1: (*Top*) Absorption spectrum of (Fe^{II}/BH_4/Trp)-TPH produced by subtracting the spectrum of the (Fe^{II}/BH_4)-TPH sample from the spectrum of (Fe^{II}/BH_4/Trp)-TPH, adapted from Fig 1. (*Bottom*) MCD spectroscopy performed at 2, 10 and 20 K at 7 T (with 0 T subtracted) on the (Fe^{II}/BH_4/Trp)-TPH sample showing a decrease in intensity with increasing temperature. This temperature dependent behavior is characteristic of a paramagnetic center (Fe^{II} in this case) being involved in the charge transfer transition.

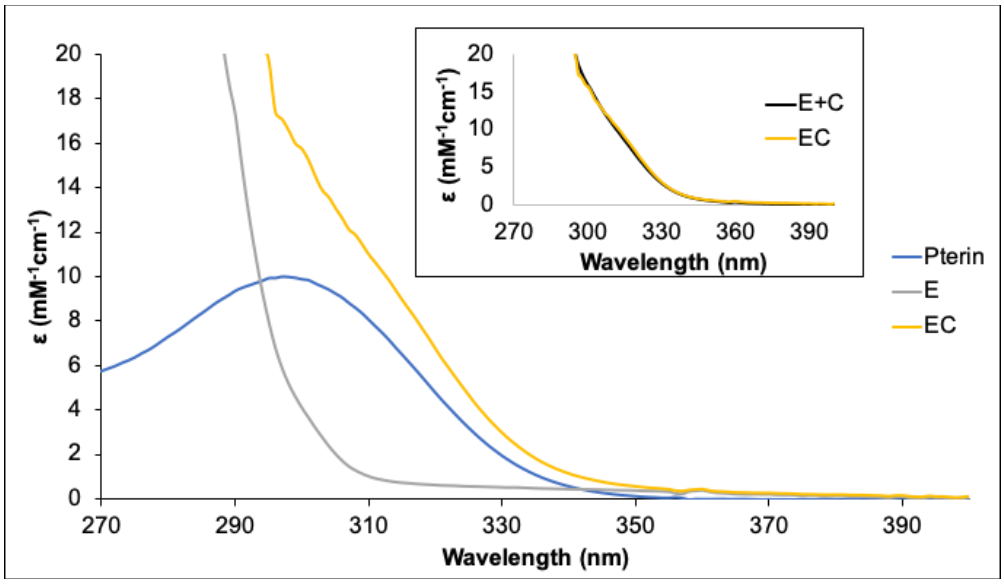

Fig. S2: Absorption spectra of 125 μM TPH (E, grey), 125 μM BH_4 cofactor (C or pterin, blue) and 125 μM (Fe^{II}/BH_4)-TPH complex (EC, yellow). *Inset.* The absorption features associated with the enzyme (grey) and the pterin cofactor (yellow) are added together (black) to reproduce the spectrum of the (Fe^{II}/BH_4)-TPH sample (yellow), demonstrating that binding of pterin to the Fe^{II}-TPH site in the absence of Trp does not result in absorption features in this energy region.

Building the Active Site Model Using Density Functional Theory (DFT)

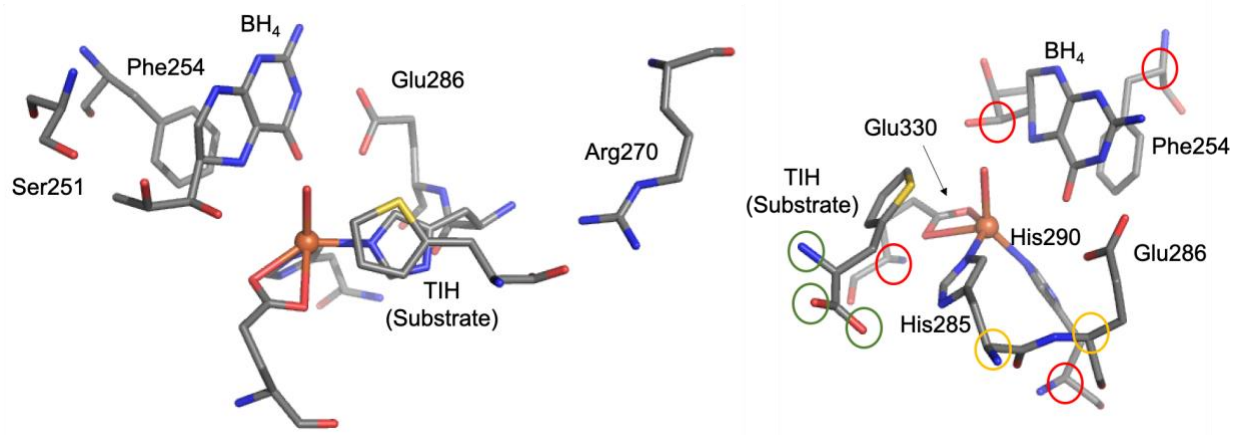

Fig. S3: *(Left)* Crystal structure of the active site of phenylalanine hydroxylase (PDB 1KW0). The residues involved in Fe^{II}, biopterin (BH_4) and β-2-thienylalanine (TIH) substrate binding/docking have been labeled. The red circles indicate the carbon atoms that were converted to methyl groups and frozen. The yellow circles indicate the side chains on the carbon atoms were converted to hydrogen atoms and the carbons were frozen. The green circles indicate the heteroatoms that were frozen.

From the crystal structure of the substrate and pterin bound active site in phenylalanine hydroxylase (Fig. S3), the iron center is bound by 2 histidines, 1 bidentate carboxylate and 1 water molecule. The pterin cofactor is hydrogen bonding to Glu286 and π-stacking with Phe254. Additionally, the terminal hydroxyl group on the pterin cofactor is hydrogen bonding to Ser251. The β-2-thienylalanine (TIH) substrate is docked by two hydrogen bonding interactions with Arg 270. From Fig. S3, to limit the size of the computational cluster models, the Arg 270 and Ser251 were not included and the C1 position on the pterin and the carboxylate O atoms on the substrate

were frozen. Additionally, Fig. S3 shows the atoms that are frozen, with the green circles representing unmodified atoms, the yellow circles indicating conversion of the prosthetic group to a $-CH_2-$ and the red circles indicating a conversion to $-CH_3$ groups.

In order to confirm the positions where the pterin and substrate were docked in the active site, pterin-Fe (4.7 Å between Fe and H on C6/C7 on pterin) and tyrosine-Fe (4.4 Å between Fe and H on C3/C5 on tyrosine) distances from pulsed electron paramagnetic resonance (EPR) studies were utilized.[12,13] Additionally, the nearest exchangeable proton in the ternary site from hyperfine sublevel correlation spectroscopy (HYSCORE) is 2.8 Å from the Fe^{II} center. Since the pulsed EPR studies were performed on tyrosine hydroxylase (TH), the active site was modified to mimic TH, where the Phe254 residue was converted to the modified tyrosine present in the TH active site[14,15] and the substrate was converted to a tyrosine. From our spectroscopic results, two active site models were considered: a model with the carbonyl on the pterin bound to the metal center and a model without the pterin bound.

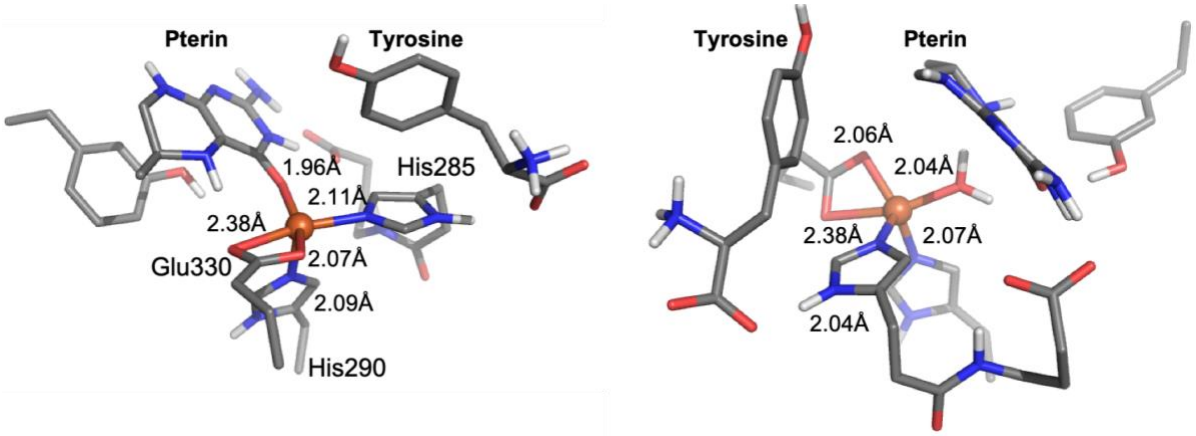

Fig. S4: (*Left*) 5-coordinate Carbonyl-bound ternary active site, with the metal-ligand bond lengths labeled. (*Right*) 5-coordinate ternary active without metal-pterin bonding. The metal-ligand bond lengths are labeled.

The facial triad residues that ligate the Fe center are His290, His285 and Glu330. The presence of a bidentate carboxylate, which has also been spectroscopically confirmed[16], along with the 2 histidine ligands account for 4 coordination positions. From MCD spectroscopy, the ternary site is 5-coordinate, thus requiring only one additional ligand to bind the iron center. When the truncated model from Fig. S3 is geometry optimized, the carbonyl on the pterin binds to the metal center with a water in the 6^{th} position. Removing the water ligand from the active site produces the model in Fig. S4, left. In order to generate a structure without the pterin carbonyl bound, the water molecule in Fig. S3 is rotated towards the pterin (to prevent its binding) and optimizes to the structure shown in Fig. S4, right. It should be noted that the ternary structure with the carbonyl bound is more stable (ΔE) by 8 kcal/mol. Both structures are within ±0.5 Å of the measured pulsed EPR distances (which was performed on the ferric-nitrosyl complex), with the carbonyl bound structure having better agreement with the experimental values.

Assignment of Ternary Complex Absorption Feature

In order to assign the charge transfer transitions observed for the ternary complex (Fig. 1A, *top*), time-dependent (TD) DFT calculations were performed. In the ternary complex (Fig. S5, *top left*), the first transition observed, above the four d→d transitions in the β-manifold, is a ligand-to-metal charge transfer (LMCT) between the pterin π and dπ* orbitals (see Fig. S5, *top right*, for valence orbital manifold and comparison with ternary site without carbonyl bound). The frontier molecular

orbitals (FMOs) for this transition are shown in Fig. S6, where the orbital overlap giving the CT intensity is along the Fe-carbonyl bond. This can also be observed by comparing the calculated TD-DFT spectra without and with the carbonyl bound (Fig. S5), where only the latter has significant LMCT intensity.

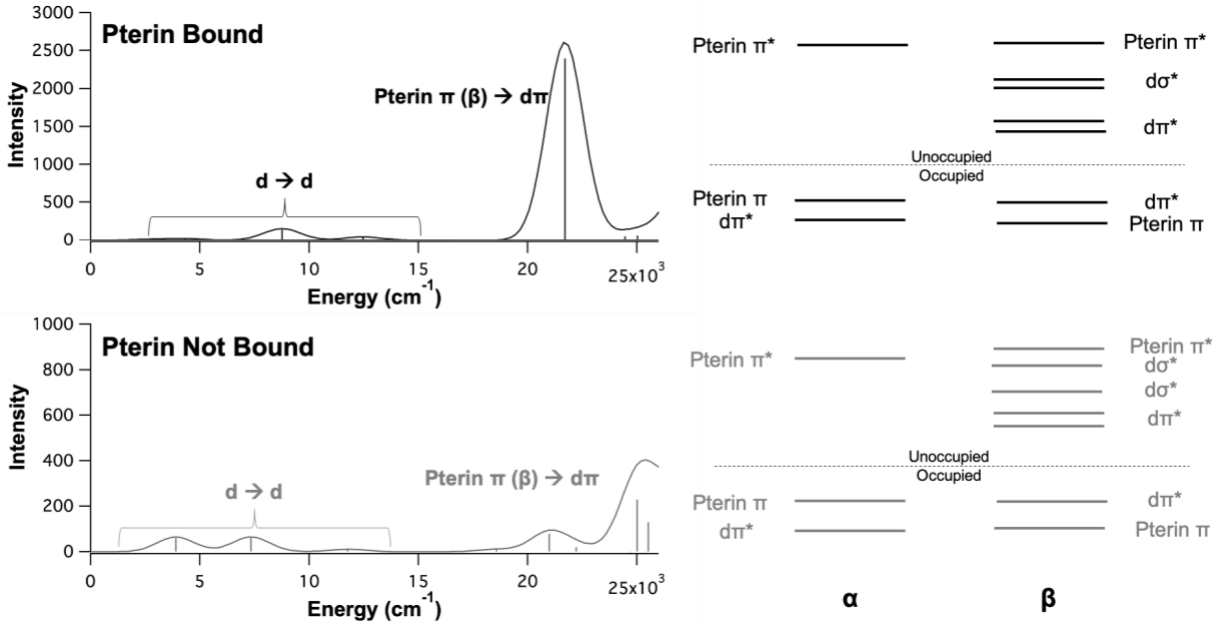

Fig. S5: (*Left*) Time-dependent DFT (TD-DFT) calculated transitions for the pterin carbonyl bound ternary complex (*Top, black*) and the ternary complex without bound pterin (*Bottom, grey*), with the donor and acceptor for each transition indicated. (*Right*) Molecular orbitals near the highest occupied molecular orbital (HOMO), lowest unoccupied molecular orbital (LUMO) gap for the pterin carbonyl bound ternary complex (*top, black*) and the ternary complex without bound pterin (*bottom, grey*). Note that the y-axis is different in the top and bottom TD-DFT spectra where the charge transfer from the pterin π to dπ is >30-fold more intense in the pterin bound calculated spectrum than the ternary complex without bound pterin.

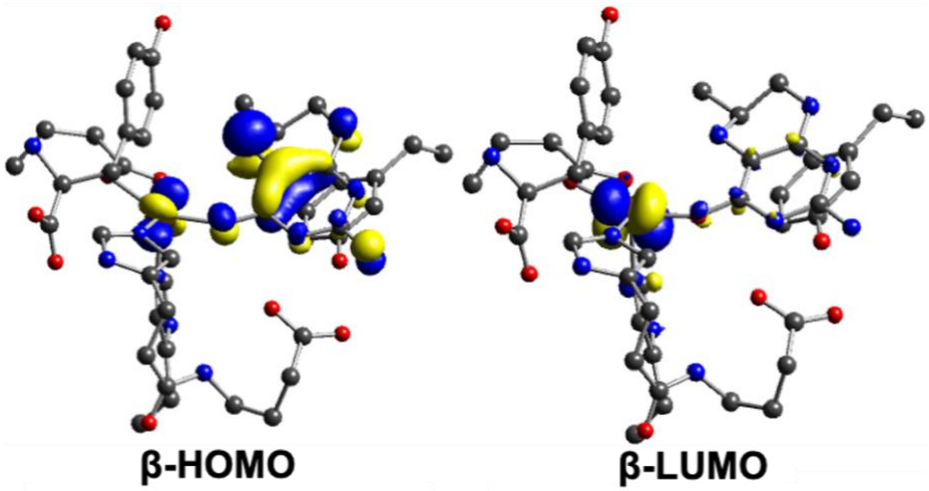

Fig S6: Contours of the donor and acceptor molecular orbitals for the ternary complex

Definition of the Vibrations Observed in the Resonance Raman Spectrum of the Ternary Complex

The pterin cofactor can either have its carbonyl group on the pyrimidine ring or its N5 amine (deprotonated) on its pyrazine ring interact directly with the metal center while performing productive chemistry. We have evaluated both possibilities below and demonstrated that only carbonyl binding reproduces the experimental resonance Raman spectrum. Note that Raman mode enhancement requires distortion along the associated normal mode of vibration in the charge transfer excited state relative to the ground state.

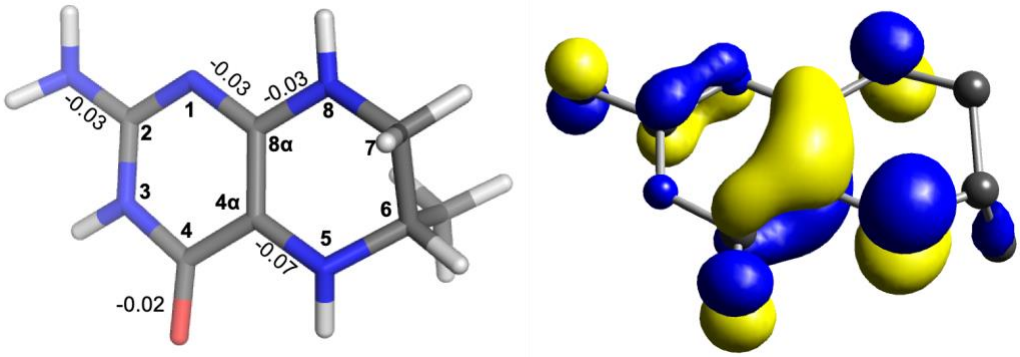

Fig. S7: (*Left*) Upon 1-electron oxidation of the reduced pterin cofactor that is protonated (see Fig. S8 for non-protonated N5 amine), there are five bond lengths that appreciably change. Three C-N bonds get shorter by 0.03 Å, the carbonyl gets shorter by 0.02 Å and the C4α-N5 bond shortens by 0.07 Å. (*Right)* LUMO contour for the oxidized pterin demonstrates that the major antibonding interactions involve the largest structural distortions, which results in resonance Raman intensity.

By performing DFT calculations on the ternary complexes with and without the pterin carbonyl bound in Fig. S4, we identified that, when carbonyl binds to the Fe^{II} center, the C-O bond elongates from 1.24 to 1.277 Å. This carbonyl elongation due to binding to the metal center reduces the calculated C=O vibration from 1726 cm^{-1} to 1663 cm^{-1}, consistent with the decrease in the highest observed vibration in the resonance Raman data on the reduced pterin to the ternary complex in Fig. 1B from 1695[17] to 1601 cm^{-1}.

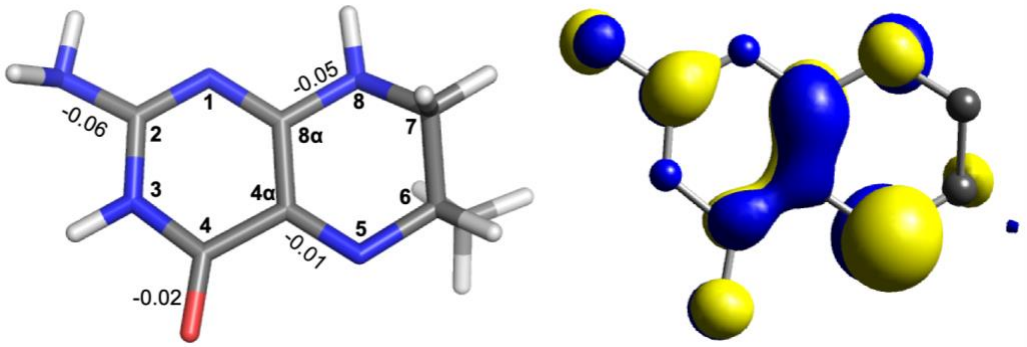

Fig. S8: (*Left*) Upon 1-electron oxidation of the reduced pterin cofactor that is deprotonated at the N5 amine, there are three bond lengths that appreciably change. The C8α-N8 bond gets shorter by 0.05 Å (C8α-N8), the carbonyl gets shorter by 0.02 Å and the C2-NH_2 bond gets shorter by 0.06 Å. (*Right)* LUMO contour for the oxidized pterin demonstrates that the major antibonding interactions involve the largest structural distortions.

By performing a frequency calculation on the deprotonated pterin cofactor, the C=O and the N8-C8α stretches are predicted at 1710 cm^{-1} and 1520 cm^{-1} respectively. These predictions do not reproduce the experimental spectrum (Fig. 1B), as there is only one observed vibration between 1400 and 1700 cm^{-1}. Furthermore, the carbonyl stretch at 1710 cm^{-1} is too high in energy relative to the 1601 cm^{-1} observed from the experimental spectrum and since the Fe^{II} is proposed to coordinate with the N5 amine in this model, the carbonyl vibration cannot decrease substantially in frequency.

Table S1: Correlation between observed resonance Raman vibrations with DFT calculated vibrations for the ternary complex. Note that the calculated reduced pterin carbonyl stretching frequency is 1726 cm^{-1}.

Observed Vibration (cm^{-1})	DFT Calculated Vibration (cm^{-1})	Assignment
510	580	Fe-$O_{Carbonyl}$ Stretch
1255	1278	Quadrant Stretch (along C4α-N5)
1601	1663	Carbonyl Stretch

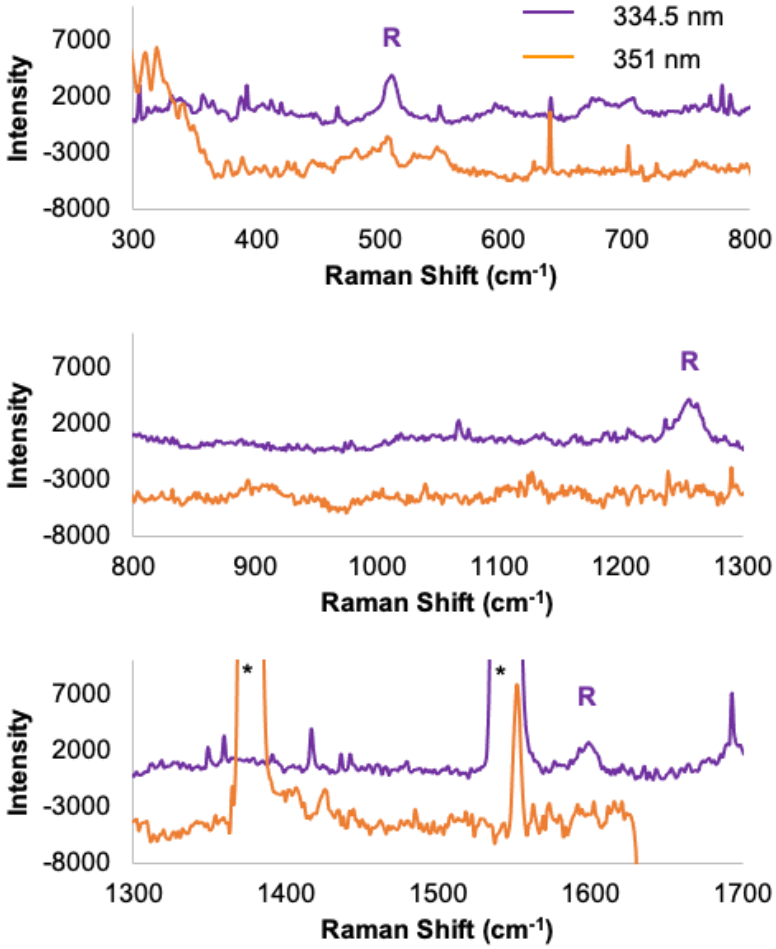

Fig. S9: Resonance Raman spectra of 0.5 mM (Fe^{II}/BH_4/Trp)-TPH obtained using the 334.5 nm (purple) and 351 nm (orange) laser lines. These data demonstrate that the 510, 1255 and 1601 cm^{-1} features are resonance enhanced (labeled R) by the 30,300 cm^{-1}. Note that the peaks marked by asterisks are due to plasma lines.

Dehydration of the Hydroxylated Pterin Cofactor

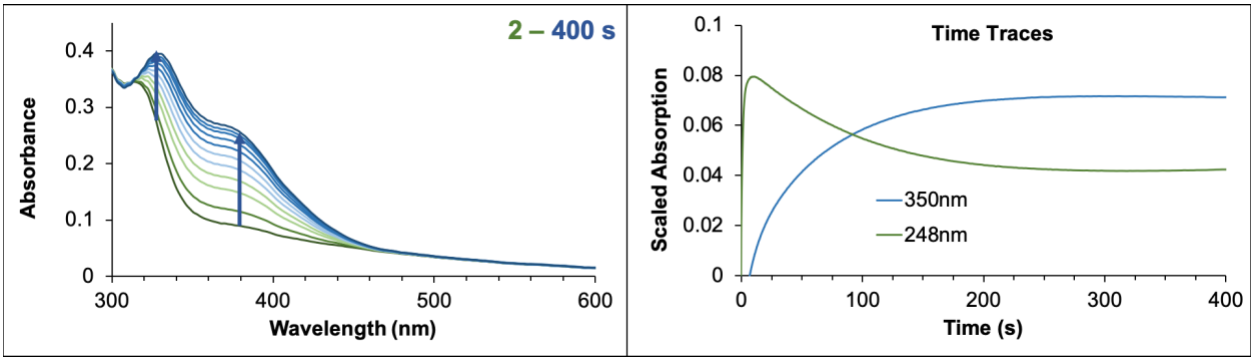

Fig S10: SF-Abs spectra monitoring the reaction of 0.125 mM (Fe^{II}/BH_4/Trp)-TPH with 1 mM O_2 in HEPES/$(NH_4)_2SO_4$/sucrose buffer (pH 7) showing (*left*) the formation of the quinonoid dihydrobiopterin product at long times.[18] (*Right*) Time traces of the reaction demonstrate that the decay of the hydroxybiopterin (248 nm) leads to the formation of the quinonoid dihydrobiopterin product (350 nm).

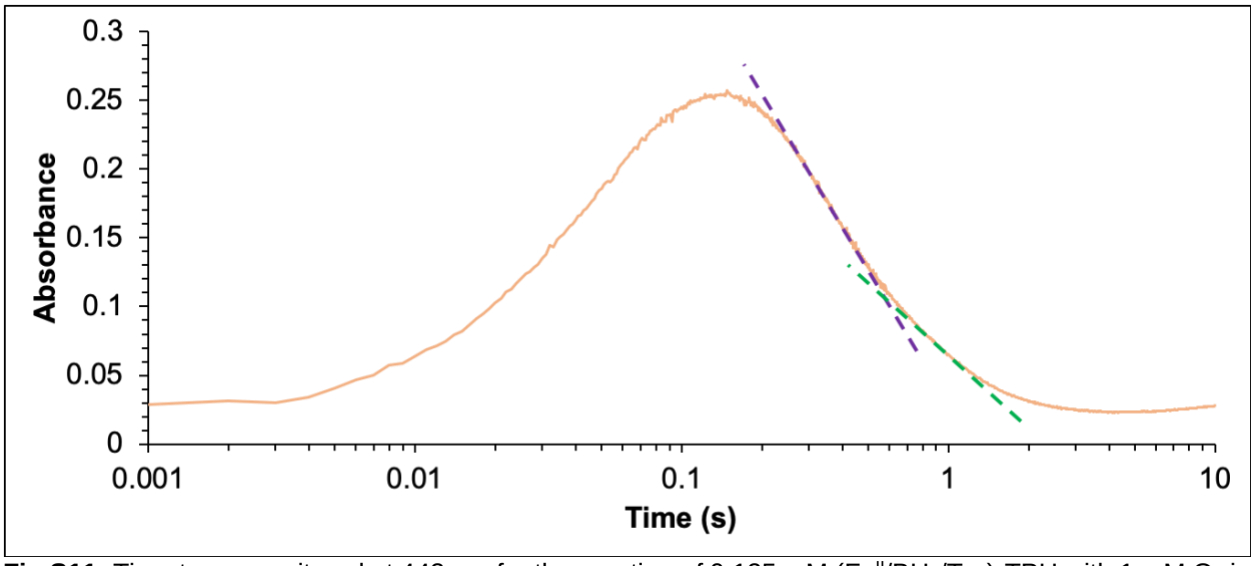

Fig S11: Time trace monitored at 442 nm for the reaction of 0.125 mM (Fe^{II}/BH_4/Trp)-TPH with 1 mM O_2 in HEPES/$(NH_4)_2SO_4$/sucrose buffer (pH 7) plotted on a log time scale showing the presence of two decay phases indicated by purple and green dashed lines. The data in H_2O/sucrose buffer are presented due to the larger separation between the two intermediate decay rate constants (Scheme 2).

Developing a kinetic model for the formation and decay of the intermediate

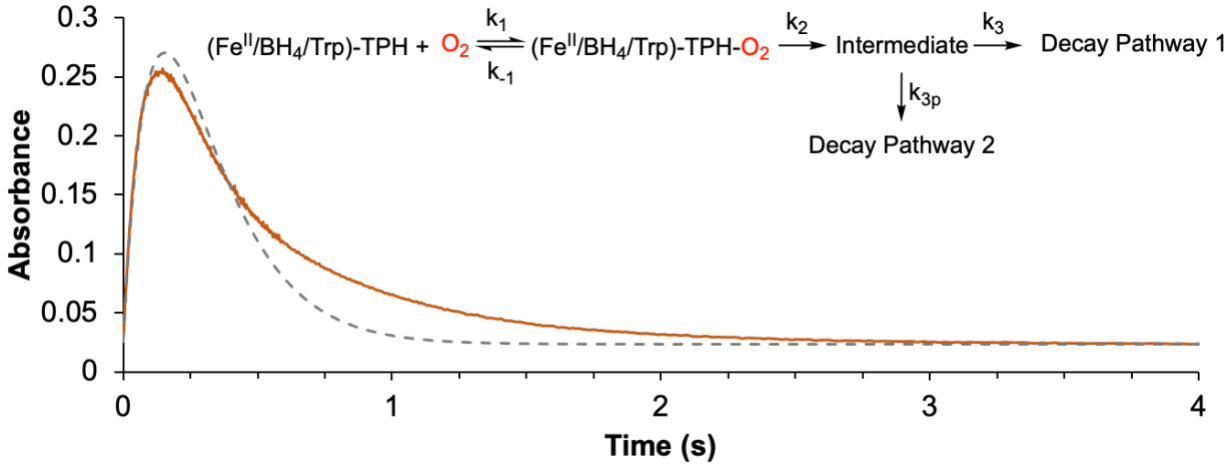

Fig S12: The 442 nm absorption data for the reaction of 0.125 mM (Fe^{II}/BH_4/Trp)-TPH with 1 mM O_2 in HEPES/$(NH_4)_2SO_4$/sucrose buffer (pH 7) best fit (grey dashed lines) to the branched decay model (*inset* shows kinetic model for the formation and decay of the O_2 dependent intermediate observed at 442 nm in stopped-flow absorption spectroscopy with two decay pathways).

From Fig. S11, there are two decay phases associated with the 442 nm intermediate, one major fast phase (purple line) between 150 and 600 ms and one minor slow phase between 600 ms and 2 s (green line). Additionally, from the time-dependent absorption spectra in Fig. 2B, the decay of this intermediate does not lead to the formation of a second species in the visible region. In order to capture the decay behavior in the absorption data, a branched (bifurcated) decay model was first explored (Fig. S12). From the simulation in Fig. S12, the second decay pathway (k_{3p}) in the model does not capture the biphasic behavior of the absorption data between 0.6 and 2 s. Additionally, if k_{3p} is much slower than k_3, most of the decay would occur through the k_3 decay pathway and would not result in the slower decay phase observed between 0.6 – 2 s. Thus, a branched decay model is not operative in this reaction.

Since the second decay phase cannot be captured by a branched model, a second formation phase for the same intermediate was evaluated through two parallel reactions. A second formation phase could be due to two different O_2 equilibrium binding constants or two different intermediate formation rates (k_2). Since the second decay phase for the intermediate (Fig. S11, green) is much slower than the first decay phase (Fig. S11, purple), a model with a fast and slow k_2 formation rate would not capture the plateau as the faster phase would dominate. Thus, two different O_2 equilibria have been modeled to fit the kinetic data as presented in Scheme 2. From the MCD and Mössbauer data presented in Fig. 1A and Fig. 3A, the ternary complex has two 5C sites (in a 60/40 ratio) with different electronic and geometric structures. The two different O_2 equilibria from the kinetic data are thus attributed to the differential O_2 binding to these two ternary sites observed from spectroscopy. Using the relative ratios for the two ternary sites, the absorption data were fit to the kinetic model in Scheme 2, with the fits shown in Figs 2D (D_2O, sucrose buffer) and S13 (H_2O, sucrose).

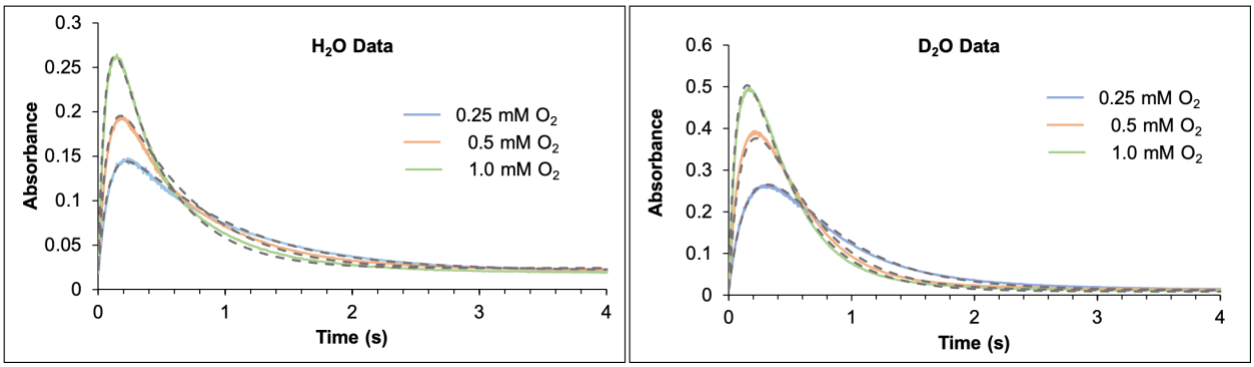

Fig. S13: Monitoring the reaction of (Fe^{II}/BH_4/Trp)-TPH in HEPES/$(NH_4)_2SO_4$/sucrose buffer (pH 7 [left, 0.125mM] and pD 7 [right, 0.15mM]) with 0.25 mM O_2 (blue), 0.5 mM O_2 (orange) and 1 mM O_2 (green) at 442nm. These time traces are fit (grey dashes) with the kinetic model presented in Scheme 2.

Computational Generation of the Peroxy Intermediates

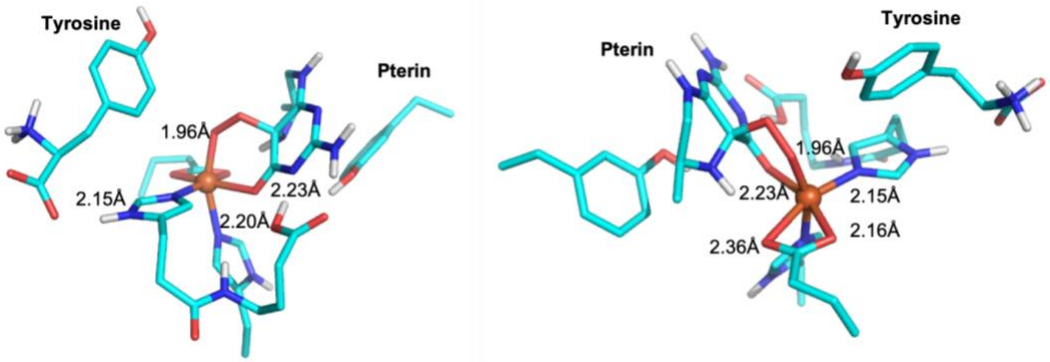

Fig. S14: Geometry optimized peroxide intermediate generated by the addition of O_2 to the ternary complex in Fig. S4 (*left*) with the **pterin carbonyl bound** to the metal center in two different orientations. The Fe-ligand bond lengths are indicated.

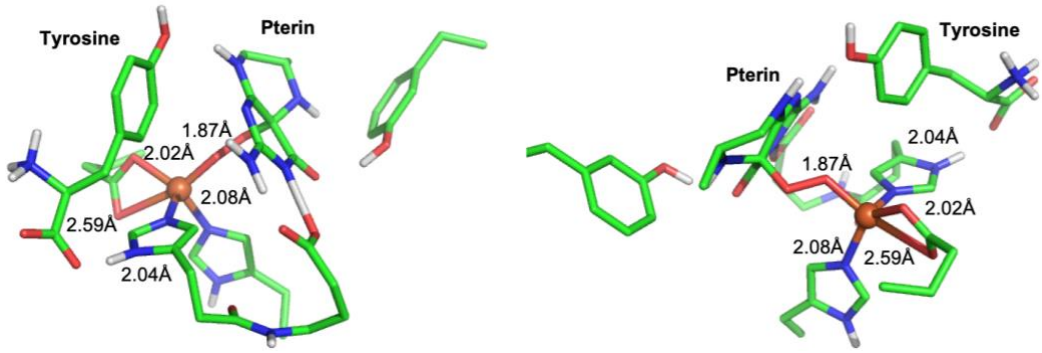

Fig. S15: Geometry optimized peroxide intermediate generated by the addition of O_2 to the ternary complex in Fig. S4 (*right*) with the **pterin carbonyl not bound** to the metal center in two different orientations. The Fe-ligand bond lengths are indicated.

Assignment of Intermediate Absorption Feature

The absorption spectrum for the pre-Fe^{IV}=O intermediate in Fig. 2A (replotted on an energy scale in Fig. S16) shows at least three overlapping transitions between 350 – 600 nm (18,000 – 28,000 cm^{-1}) with the most intense feature at 442 nm and weaker features on both the lower and higher energy side of this main transition. From the TD-DFT calculation on the carbonyl bound peroxo model, three transitions are calculated to be in this region (Fig. S17, *top left*). All the transitions involve the pterin π LUMO (Fig. S17, *top right*), since the pterin π is unoccupied in the peroxo intermediate relative to the ternary complex, as it has reduced O_2 by two electrons. The most intense feature is the dπ*(β) to pterin π metal-to-ligand CT (MLCT) transition, while the two weaker transitions are interligand transitions in the α and β manifolds from the occupied peroxo π* to the unoccupied pterin π orbital. As the resonance Raman vibrations show small O_2 isotope dependence, the intense feature in the absorption spectrum (at 442 nm) is assigned as the dπ* → pterin π transition, with the other two components being the peroxide π* → pterin π transitions. Comparing the calculated TD-DFT spectra with and without the carbonyl bound to the metal center (Fig. S17, *bottom*), the direct carbonyl bond leads to higher absorption intensity by a factor of 6 and correlates with the experimental molar extinction coefficient of 5,500 $M^{-1}cm^{-1}$.

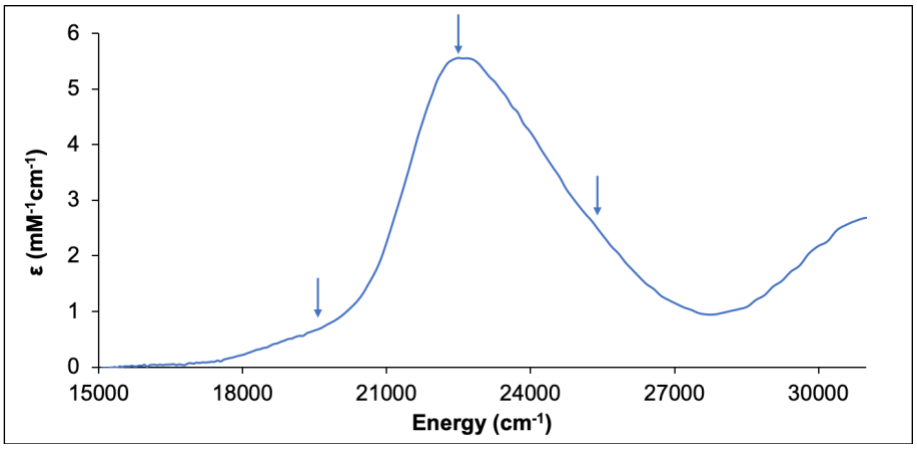

Fig. S16: Peroxy intermediate spectrum replotted on an energy scale. This shows the presence of at least three absorption features between 18,000 and 27,000 cm^{-1} indicated by arrows.

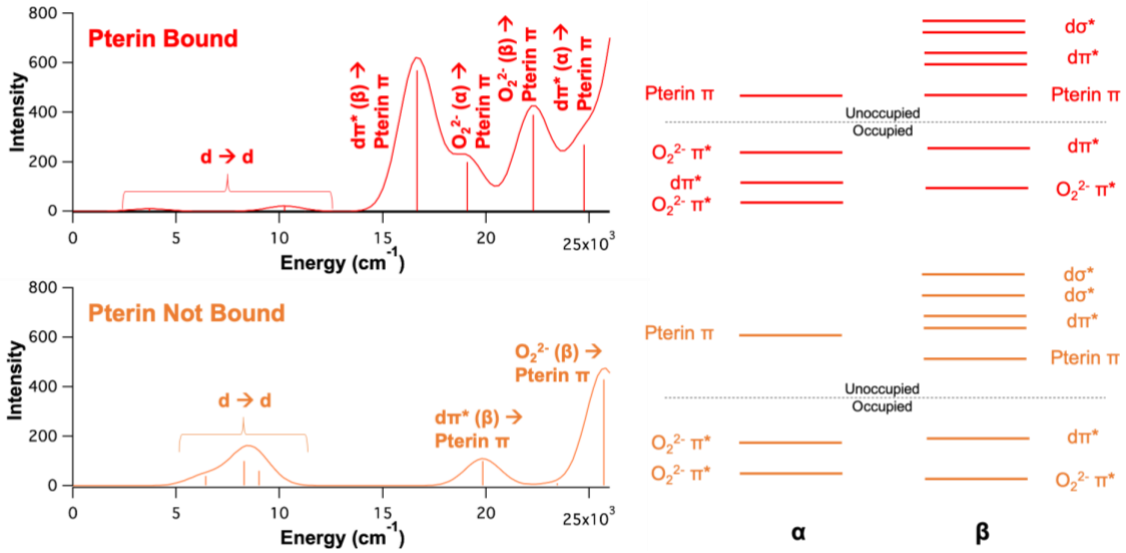

Fig. S17: (*Left*) TD-DFT calculated transitions for the pterin carbonyl bound peroxo intermediate (*Top, red*) and the peroxo without bound pterin (*Bottom, orange*), with the donor and acceptor for each transition indicated. (*Right*) Molecular orbitals near the HOMO, LUMO gap for the peroxo intermediate with (*top, red*) and without bound pterin (*bottom, orange*). Note that TD-DFT spectrum with the carbonyl bound charge transfer is more intense than the peroxo without bound pterin.

Resonance Enhanced Features Associated with the Intermediate

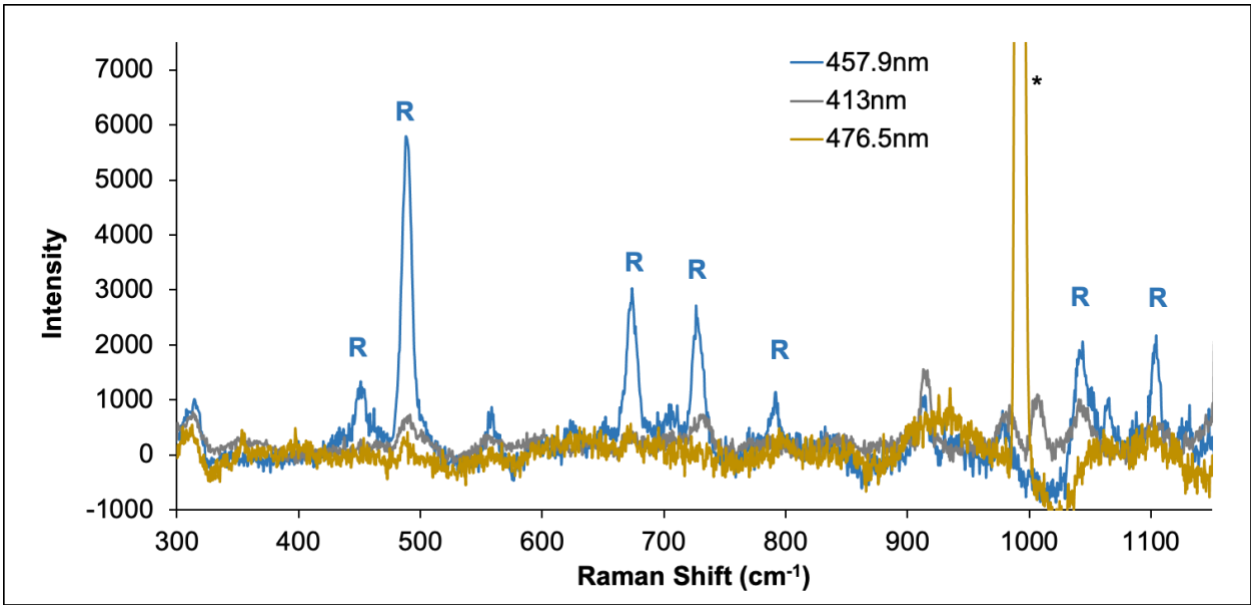

Fig. S18: Resonance Raman spectra (0.5 mM (Fe^{II}/BH_4/Trp)-TPH + 1 mM O_2) obtained using the 413 nm, 457.9 nm and 476.5 nm laser lines on the intermediate rapid-freeze quenched at 150 ms. These data demonstrate that the 451, 489, 674, 727, 792, 1041 and 1103 cm^{-1} features are resonance enhanced (labeled R). Note that the peak marked by the asterisk is due to a plasma line.

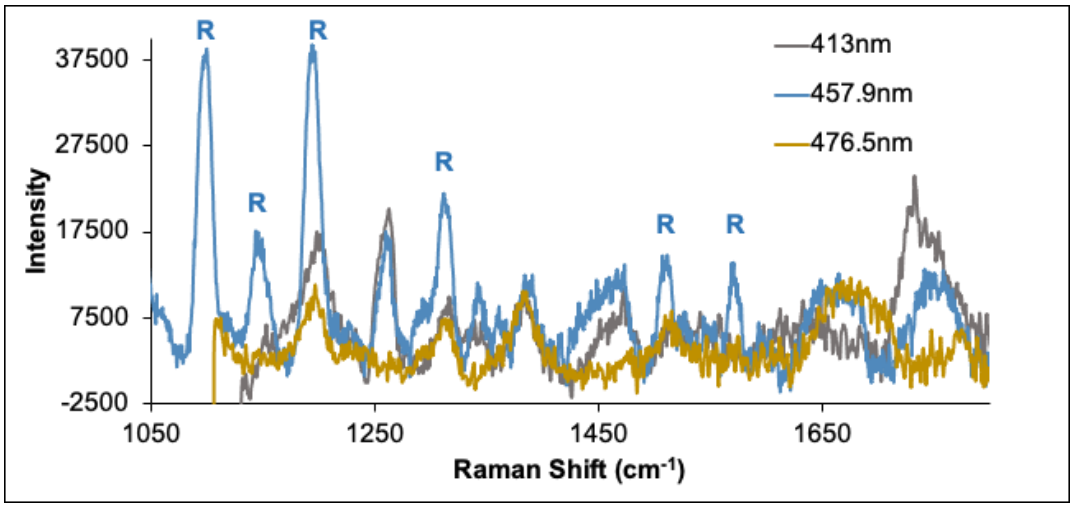

Fig. S19: Resonance Raman spectroscopy (0.5 mM (Fe^{II}/BH_4/Trp)-TPH + 1 mM O_2) performed using the 413 nm, 457.9 nm and 476.5 nm laser lines on the intermediate rapid-freeze quenched at 150ms. These data demonstrate that the 1156, 1195, 1314, 1514 and 1570 cm^{-1} features are resonance enhanced. Note that the feature at 1103 cm^{-1} is used as a reference from Fig. S8 to demonstrate the relative intensities of the features between 1100 and 1600 cm^{-1}.

Assignment of the Intermediate Vibrational Features

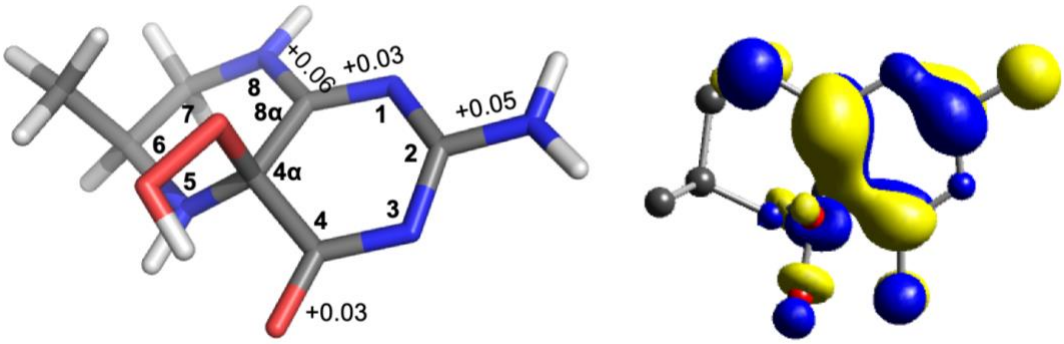

Fig. S20: (*Left*) Upon 1-electron reduction of the hydroperoxylated pterin cofactor, there are four bonds that appreciably change. The carbonyl elongates by 0.03 Å, the C-NH_2 bond elongates by 0.05 Å, the C8α-N1 bond elongates by 0.03 Å and the C8α-N8 bond elongates by 0.07 Å. (*Right)* LUMO contour for the reduced pterin-hydroperoxide demonstrates that the major antibonding interactions involve the largest structural distortions (as listed).

In order to assign the resonance Raman data, we compared frequency calculations on the Fe^{II}-peroxy intermediate with and without the pterin carbonyl bound to the metal center. The vibrations in the metal-ligand region are assigned based on the observed $^{16/18}O_2$ isotope perturbations in the experimental data. As the 442 nm absorption feature is a Fe^{II}-to-oxidized pterin charge transfer transition, the most intense metal ligand vibration is the Fe-$O_{carbonyl}$ at 489 cm^{-1} and has a small O_2 isotope effect due to its mixing with the peroxo via an $O_{carbonyl}$-Fe-$O_{peroxide}$ bending mode of the six-membered ring as shown (Fig. S21). The 451 cm^{-1} is the Fe-$O_{peroxide}$ stretch, which mixes with the Fe-$O_{carbonyl}$ stretch, causing its $^{18}O_2$ isotope effect (calculated to be 16 cm^{-1} for a pure Fe-O stretch) to distribute over several vibrational modes due to mixing in the ring structure. Finally, the vibration at 792 cm^{-1} is the C_4-$C_{4\alpha}$ stretch that mixes with the peroxo O-O stretch, thus exhibiting a small isotope perturbation. From the calculated vibrations for the peroxo intermediate, the two resonance enhanced non-isotope dependent features at 674 and 727 cm^{-1} are calculated to be

in-plane and out-of-plane six-membered ring distortions respectively. The combination of these modest O_2 isotope effects and the in-plane and out-of-plane distortions require simultaneous O_2 and carbonyl binding to the iron center. In the 1500 – 1600 cm^{-1} region, the carbonyl vs C=N stretch (Fig. S20) was assigned based on the reduction in computational frequencies due to carbonyl coordination to the metal center. Due to the six-membered ring constraint in addition to the longer C=O bond (~0.02 Å) due to metal coordination, the carbonyl stretch substantially decreases in frequency while the C=N does not significantly perturb. This leads to the carbonyl stretch being assigned as the 1514 cm^{-1} vibration and the C=N stretch as the 1570 cm^{-1} feature, as indicated in Table S2.

Table S2: Correlation between observed resonance Raman vibrations with DFT calculated vibrations for the intermediate. The vibrations in the metal-ligand region are assigned based on the observed small $^{16/18}O_2$ isotope perturbations and confirmed using a frequency calculation on the peroxide intermediate (Fig. S14).

Observed Vibration (cm^{-1}) ($^{16}O_2$ – $^{18}O_2$)	DFT Calculated Vibration (cm^{-1}) ($^{16}O_2$ – $^{18}O_2$)	Assignment
451 (5)	408 (6)	Fe-O_{Peroxy} Stretch
489 (3)	442 (3)	Fe-$O_{Carbonyl}$ Stretch
674	711	In-plane Fe-Peroxy-Pterin Ring Stretch
727	756	Out-of-plane Fe-Peroxy-Pterin Ring Stretch
792 (5)	861 (6)	C_4-$C_{4\alpha}$ Stretch
1514	1631	Carbonyl Stretch
1570	1686	C=N Stretch

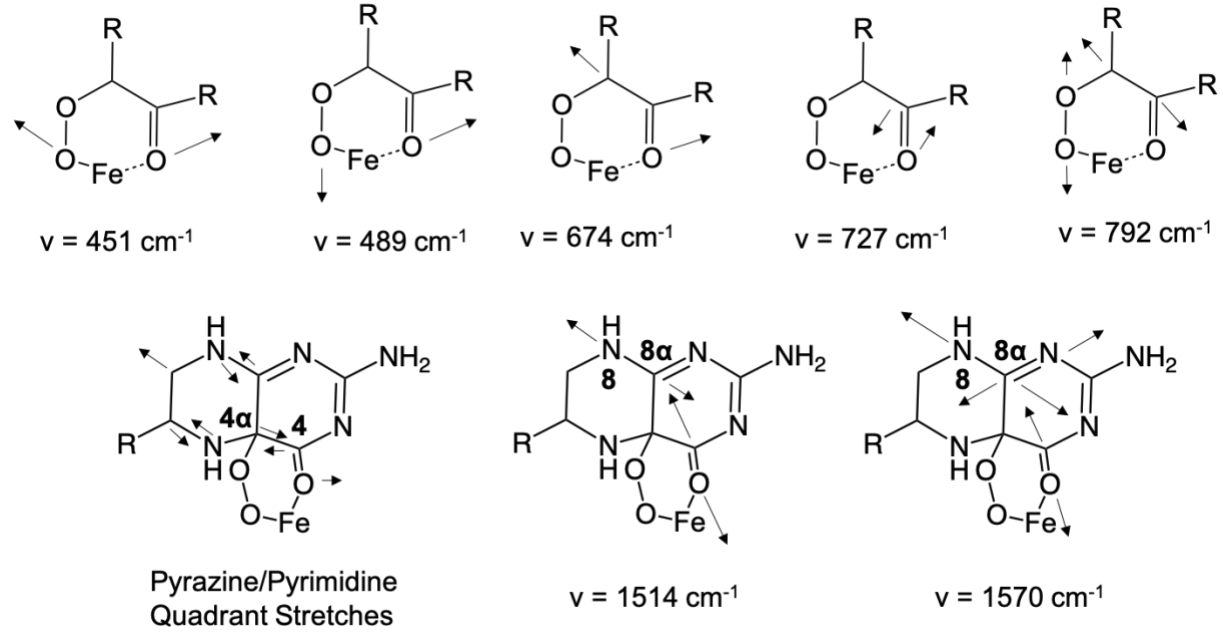

Fig. S21: Vibrational Assignments for the intermediate in the metal-ligand region (*top*) and the intra-pterin region (*bottom*). The pterin atoms participating in the high energy vibrations are indicated. From Raman experiments on the reduced and oxidized cofactors, the vibrations in the 1000-1300 cm^{-1} are pyrazine and pyrimidine ring quadrant stretches.[17] As these quadrant stretches are in-plane vibrations, their resonance enhancement is due to the distortions along the Fe-$O_{Carbonyl}$-C_4 angle and the Fe-$O_{Carbonyl}$-C_4-$C_{4\alpha}$ dihedral, both consistent with a direct interaction between the carbonyl and the iron center.

Concentration correction for Intermediate Nuclear Resonance Vibrational Spectroscopy (NRVS) Spectrum

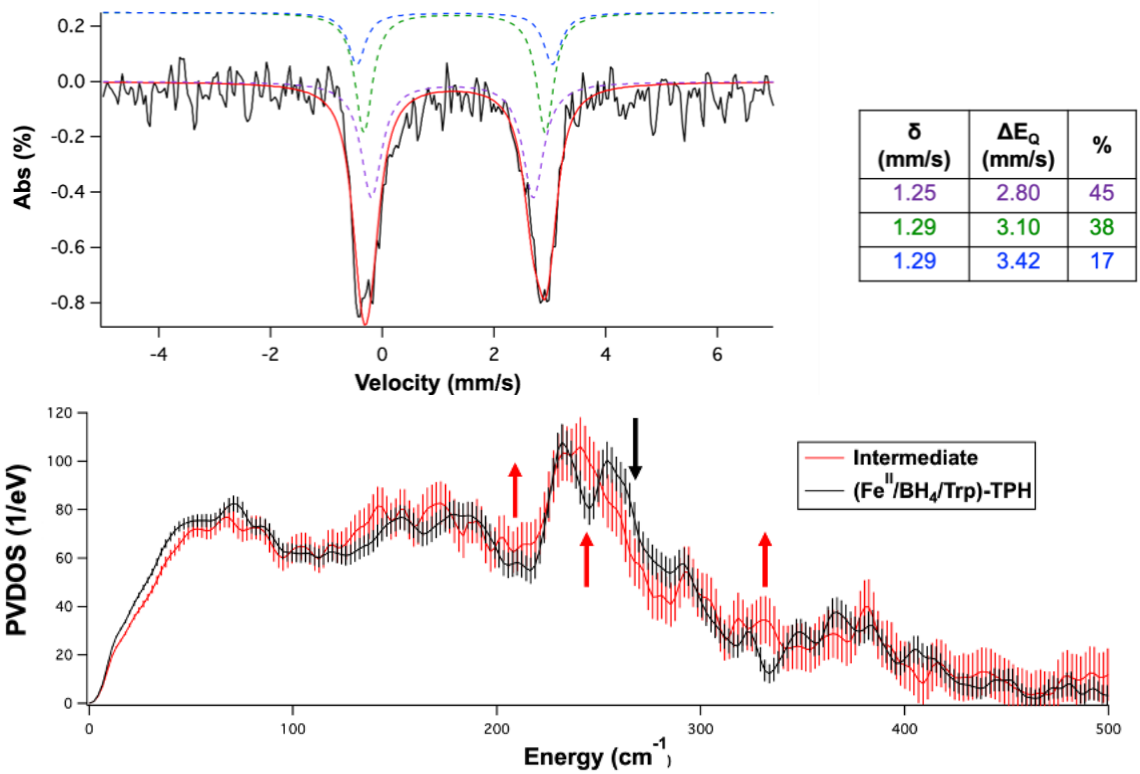

Fig. S22: *(Top)* Mössbauer spectrum of the NRVS sample of the intermediate rapid freeze quenched at 150 ms. Reaction Conditions: 1 mM (Fe^{II}/BH_4/Trp)-TPH with 1 mM O_2 in HEPES/$(NH_4)_2SO_4$/sucrose (pD 7). At these reaction conditions, the intermediate accumulates to 45% of the total iron concentration in solution, which is less than Fig. 3B because of the increase in protein concentration. (*Bottom)* Processed NRVS spectra for the intermediate (red) and the starting complex (black). The error bars in the processed spectra are represented by vertical lines. The contribution of the ternary complex to the intermediate spectrum was corrected by subtracting 55% of the ternary spectrum from the intermediate spectrum and then renormalizing it to 3 (as shown in Fig. 3D). The changes observed in the spectrum as constant before and after subtraction.

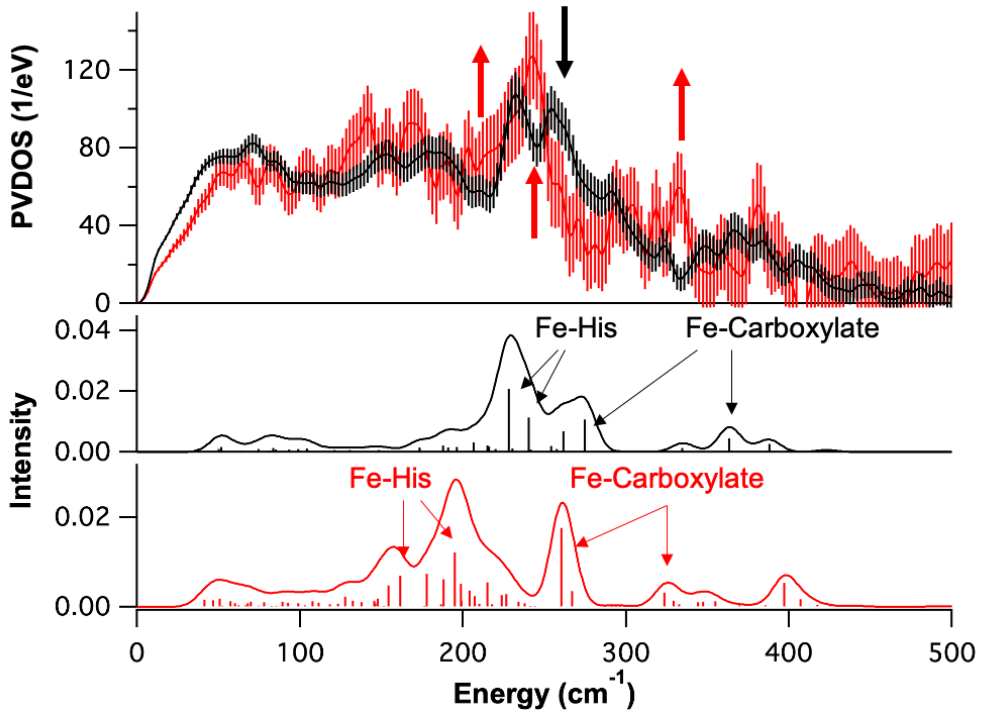

Fig. S23: (*Top*) NRVS spectra of the ternary Fe^{II} complex and the rapid freeze quenched intermediate (1 mM (Fe^{II}/BH_4/Trp)-TPH + 1 mM O_2). The error bars in the processed spectra are represented by vertical lines. The contribution of the ternary complex to the intermediate spectrum was removed as described in Fig. S22. The red arrow depicts loss of intensity while the green arrows show gain in intensity going from the ternary Fe^{II} complex to the intermediate spectrum. (*Bottom*) Simulation of NRVS spectra of the ternary complex (black) and the peroxy intermediate (red) for the model without the pterin carbonyl bound (Fig. S4, right and S15). In these simulations, the Fe-Carboxylate and Fe-His stretches for the ternary complex and peroxo intermediate are both similar in energy (black vs red arrows). Additionally, as both complexes are five-coordinate (with the Fe-carboxylate bond trans to the peroxide substantially elongated [2.6 Å] in Fig. S15), the metal-ligand bond lengths are similar and thus the spectral intensities of the Fe-His and Fe-carboxylate modes are not redistributed. This model does not reproduce the changes in the experimental NRVS spectrum, where intensity is redistributed from 260 cm^{-1} to 200-220, 240 and 325 cm^{-1}.

Two-Dimensional (2D) Potential Energy Surfaces (PES) To Form Peroxide Species

In order to generate the O_2 reaction coordinates for a model with the pterin carbonyl bound and another without bound pterin carbonyl, the ternary structures in Fig. S4 were used. Both these ternary sites are 5C and O_2 was bound to the open coordination position. In the ternary model with the pterin carbonyl bound, this coordination position is opposite (trans) to a histidine residue (resulting in a 6C superoxide), whereas for the model without bound carbonyl, this coordination position is opposite the bidentate carboxylate and the ternary site water ligand has now dissociated from the metal center, which results in a 5C superoxide. From both these superoxide structures, the peroxide complexes were generated by contraction of the O_{Distal}-$C_{4\alpha}$ bond from ~3 Å to 1.46 Å along with the deprotonation from the N_3 amine of the pterin cofactor. For both coordinates, from the respective superoxide structures, two-dimensional (2D) potential energy surfaces (PES) were calculated by contracting the O_{Distal}-C4α distance by 0.1 Å and elongating the $N_{3,pterin}$-H distance by 0.1 Å to the carboxylate.

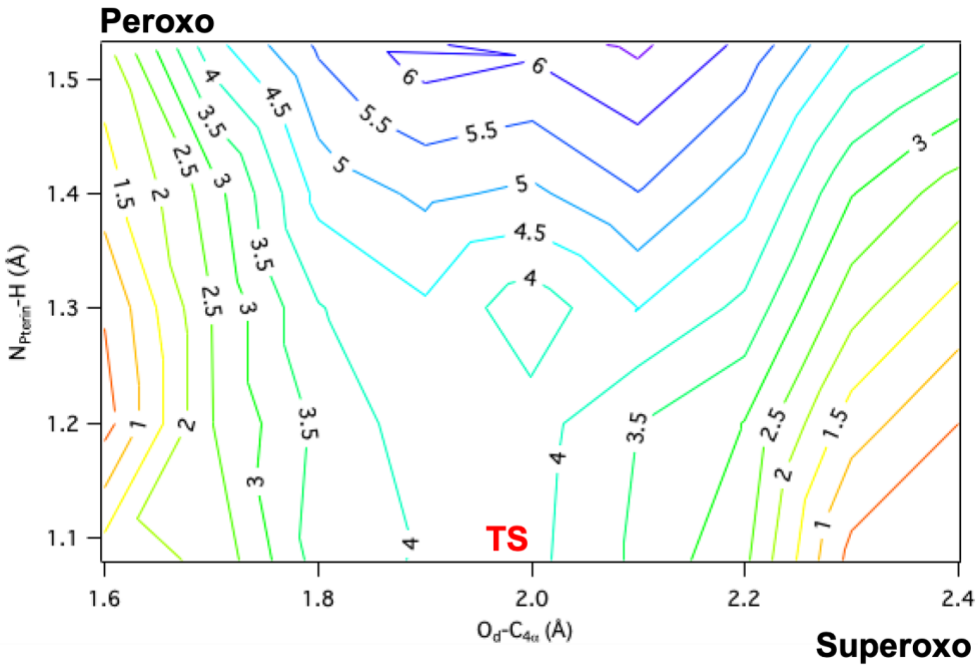

Fig. S24: 2D potential energy surface going from the superoxo (bottom, right) to the peroxo (top, left) in the **carbonyl bound reaction coordinate**. Going from the superoxo to the peroxo, the distal oxygen of the superoxide is attacking the $C_{4\alpha}$ position on the pterin (x-axis) and the proton on the pterin N_3 amine is transferring to a carboxylate residue (y-axis, see Fig. 3B). The transition state for this reaction coordinate is indicated at a C-O distance of 1.97 Å and N-H distance of 1.08 Å.

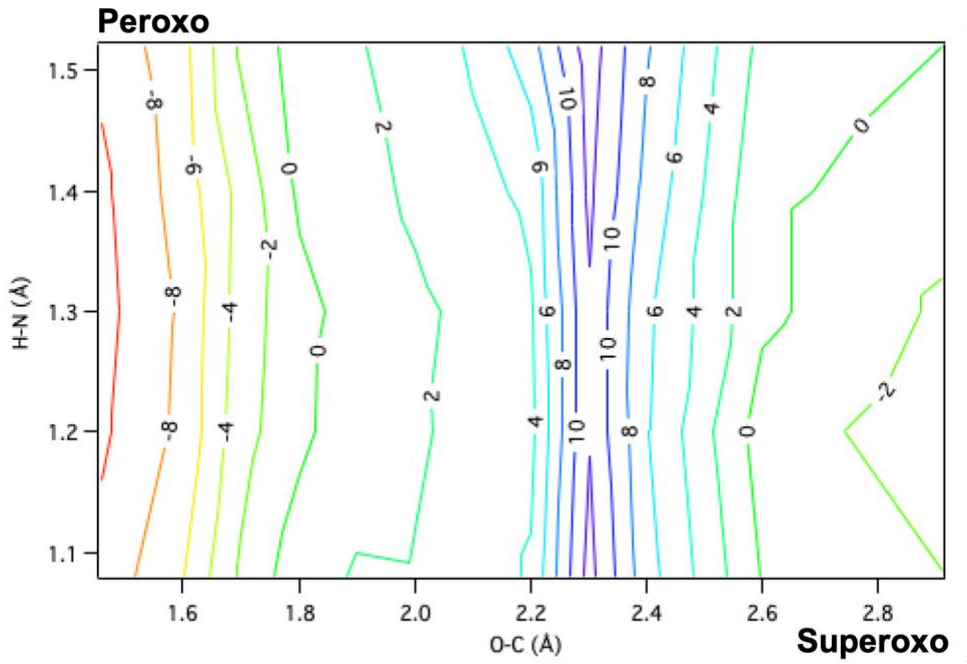

Fig. S25: 2D potential energy surface going from the superoxo (bottom, right) to the peroxo (top, left) in the **reaction coordinate without carbonyl bound**. Going from the superoxo to the peroxo, the distal oxygen of the superoxide is attacking the $C_{4\alpha}$ position on the pterin (x-axis) and the proton on the pterin N_3 amine is transferring to a carboxylate residue (y-axis, see Fig. 3B). From this potential energy surface, the transition state is likely at an O-$C_{4\alpha}$ distance of ~2.3 Å.

Impact of Direct Pterin Coordination to Iron on Electron Transfer Pathways for O_2 Activation

In order to analyze the electronic structure of each species along the two reaction coordinates and to assess the relative amounts of electron transfer between the Fe, O_2 and pterin, the spin density, charge and wavefunction composition of the frontier molecular orbitals (FMOs) were evaluated. While calculating the Mulliken charge and spin density of Fe, O_2 and pterin is relatively straightforward for the optimized structures, the wavefunction composition was calculated by decomposing each cluster model into four components, i.e. Fe, O_2, Pterin and other atoms. A Mulliken population analysis was then performed to evaluate the contribution of each fragment to the relative FMOs (using QMForge) to provide a detailed description of the electronic structure and the relative degrees of electron donation and transfer as described below. The analyses below lead to the qualitative schemes in Fig. 4C and 4D.

Electronic Structure of Ternary Complex

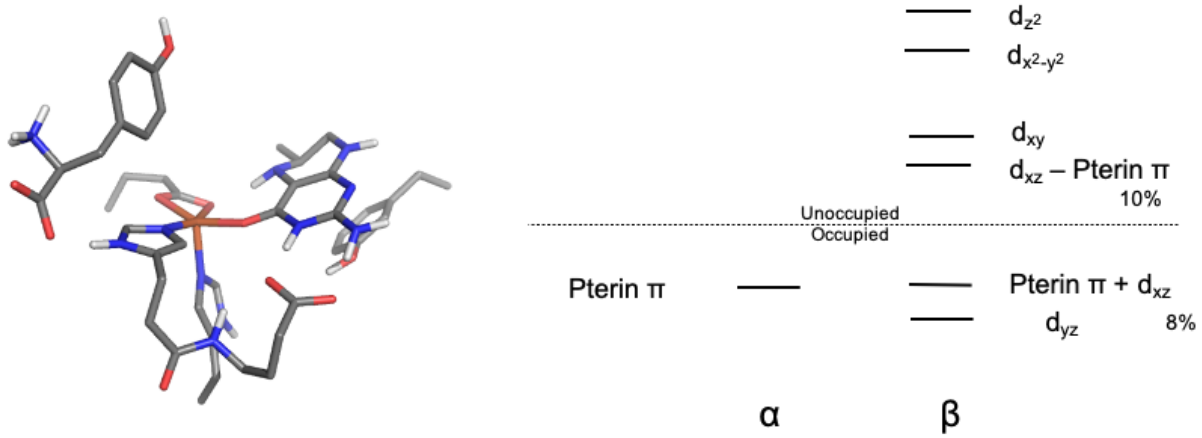

Fig. S26: (Left) Structure of the ternary active site with carbonyl bound. (Right) α and β FMOs showing mixing of pterin π and iron d_{xz}. The pterin is donating ~10% of its electron density, consistent with the pterin fragment having a charge of 0.07 and spin density of 0.09.

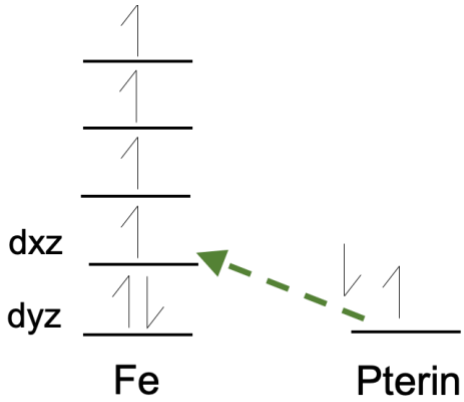

Fig. S27: Electronic structure and electron transfer pathway for the carbonyl bound ternary complex. The location of the β spin along the green arrow indicates the extent of electron delocalization.

Septet vs Quintet Superoxide

Fig. S28 presents the electronic structure of the septet superoxo and Fig. S29 presents the quintet superoxo. The quintet structure is more stable by 1.5 kcal/mol and has been evaluated in the reaction coordinates.

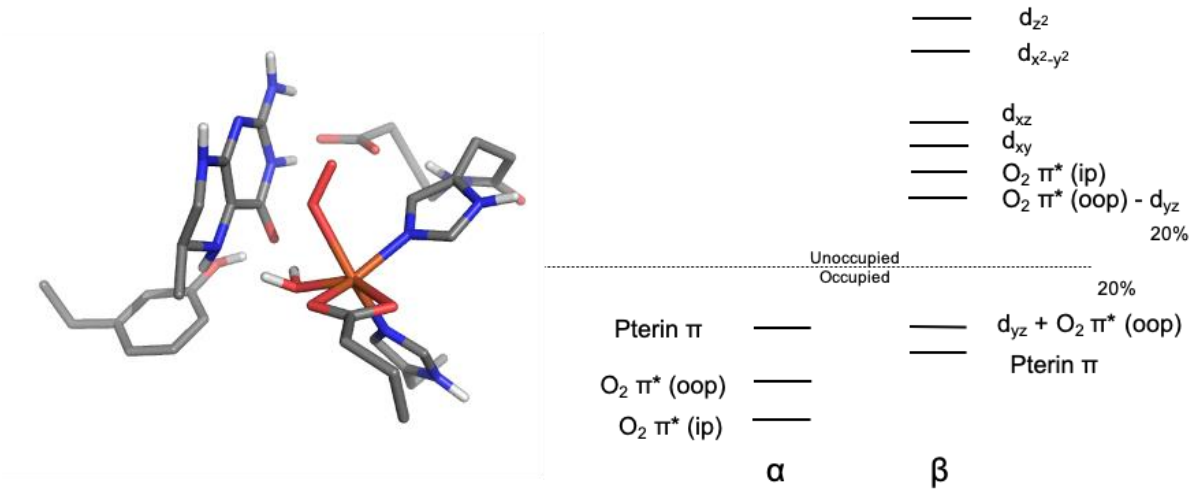

Fig. S28: (Left) Structure of the septet superoxo active site without carbonyl bound. (Right) α and β FMOs showing mixing of O_2 and iron d_{xz}. The Fe is donating ~20% of its electron density to the O_2, consistent with the O_2 fragment having a charge of -0.20 and spin density of 1.70.

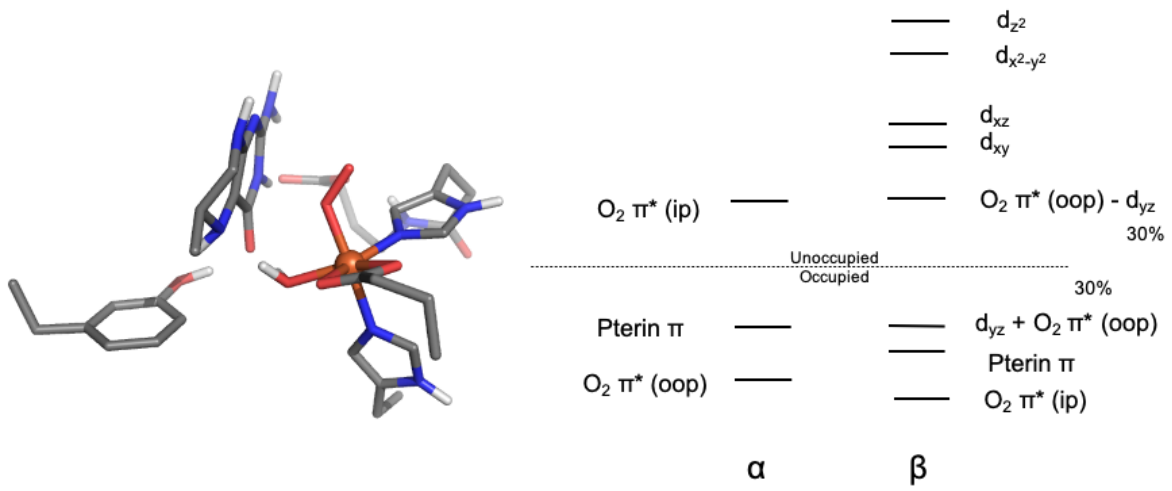

Fig. S29: (Left) Structure of the quintet superoxo active site without carbonyl bound. (Right) α and β FMOs showing mixing of O_2 and iron d_{xz}. The Fe is donating ~30% of its electron density to the O_2, consistent with the O_2 fragment having a charge of -0.26 and spin density of -0.04.

Comparing Superoxo Electronic Structures With and Without Pterin Coordination of Fe

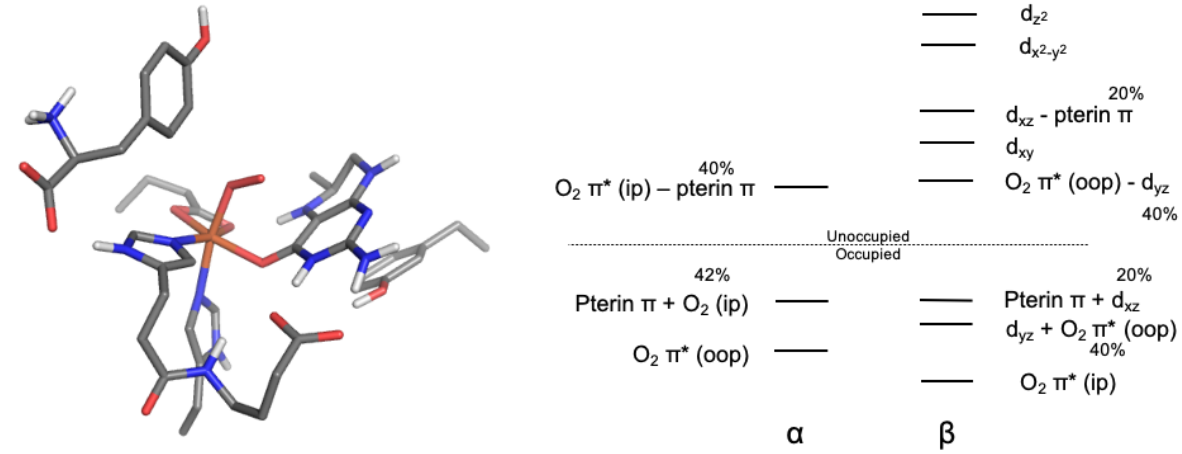

Fig. S30: (*Left*) Structure of the superoxo active site with carbonyl bound before the 2D PES. (*Right*) α and β FMOs showing mixing of O_2, pterin π and iron dπ. The pterin is donating ~20% of its electron density to the d_{xz} in the β manifold, while the iron d_{yz} electron is donated ~40% to the O_2. In the α manifold, the pterin π is ~40% donated to the superoxo π*. Collectively, these contributions are consistent with the pterin fragment having a charge of 0.47 and spin density of -0.39 and the O_2 fragment having a charge of -0.43 and a spin density of 0.40.

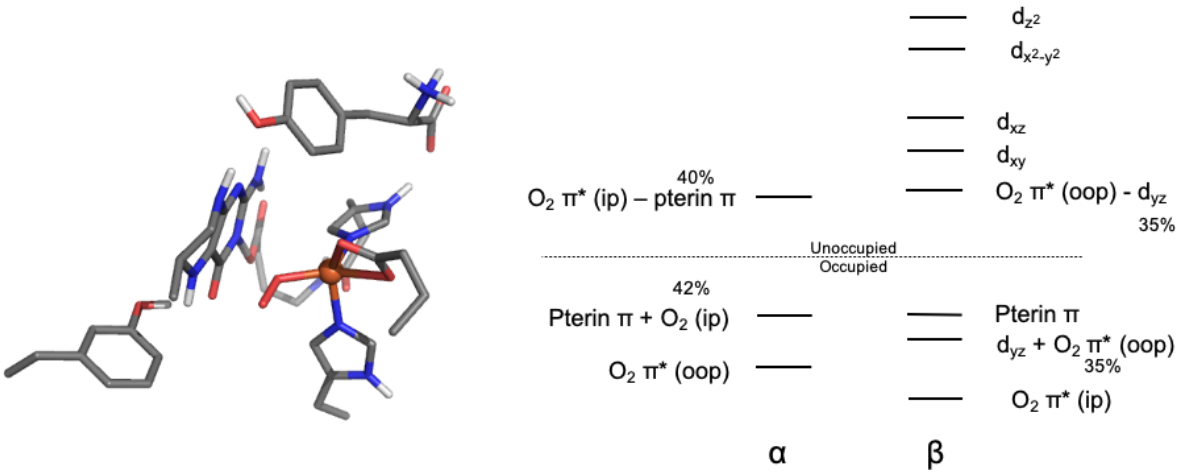

Fig. S31: (*Left*) Structure of the superoxy active site without carbonyl bound. (*Right*) α and β FMOs showing mixing of O_2, pterin π and iron dπ. The iron β-d_{yz} electron is ~35% to the O_2. In the α manifold, the pterin π is ~40% donated to the superoxo π*. Collectively, these contributions are consistent with the pterin fragment having a charge of 0.43 and spin density of -0.61 and the O_2 fragment having a charge of -0.57 and a spin density of 0.57.

Comparing Transition State Electronic Structures With and Without Pterin Coordination of Fe

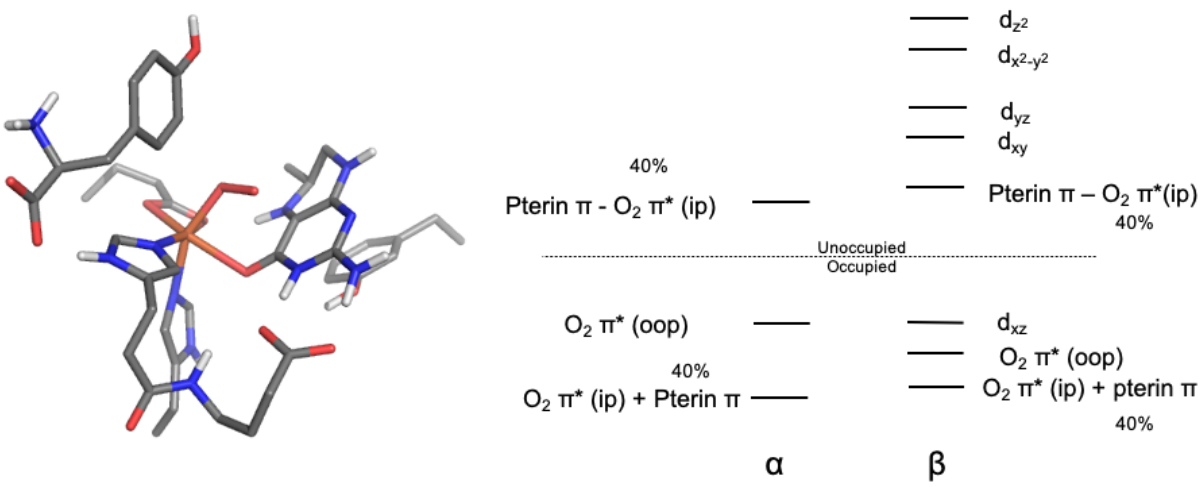

Fig. S32: (*Left*) Structure of the TS for the reaction coordinate with carbonyl bound. (*Right*) α and β FMOs showing mixing of O_2, pterin π and iron dπ. The pterin has transferred its β electron to the d_{xz}, while the iron d_{yz} electron has transferred to the O_2. In the α and β manifolds, the pterin π is interacting with the O_2 and has ~40% mixing. Collectively, these contributions are consistent with the pterin fragment having a charge of 0.74 (has not deprotonated) and spin density of 0.03 and the O_2 fragment having a charge of -0.65 and a spin density of 0.07.

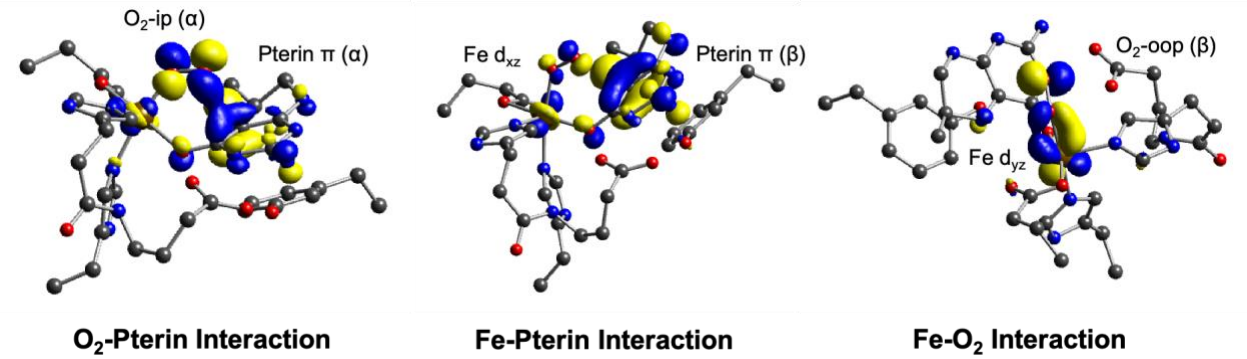

Fig. S33: Occupied contours showing the interactions between the O_2, pterin and Fe fragments. O_2-ip = O_2 in-plane and O_2-oop = O_2 out-of-plane.

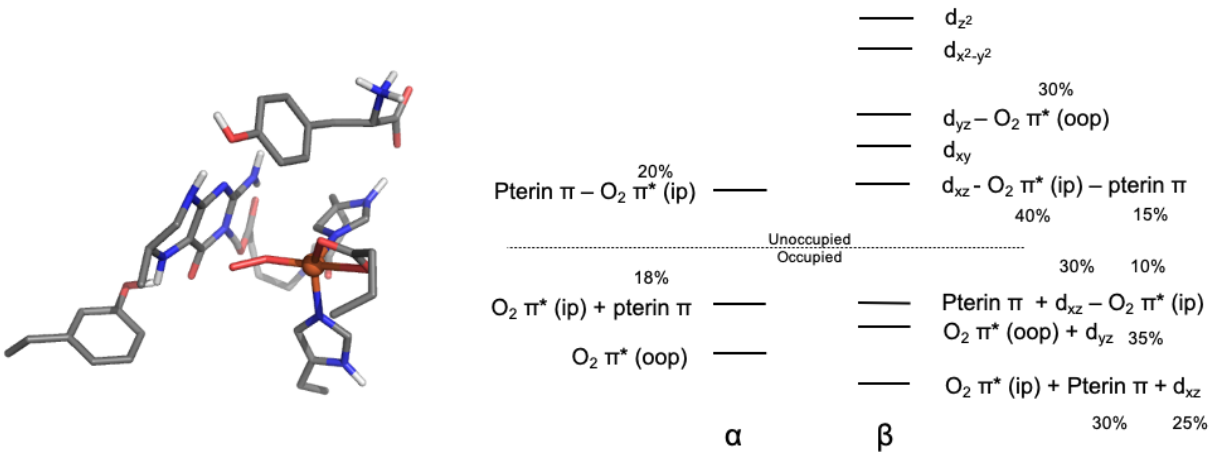

Fig. S34: (*Left*) Structure of the TS of active site without carbonyl bound. (*Right*) α and β FMOs showing mixing of O_2, pterin π and iron dπ. In the α manifold, the pterin α electron has ~80% transferred to the O_2. The iron β-d_{yz} electron is ~70% to the O_2. There is a three orbital two electron process between the Fe d_{xz}, O_2 π* and pterin π orbitals. From the orbital coefficient, the pterin electron is ~40% transferred to the O_2 and the O_2 in-plane π* electron is 45% transferred to the Fe d_{xz}. Collectively, these contributions are consistent with the pterin fragment having a charge of 0.09 (with partial proton transfer) and spin density of -0.60 and the O_2 fragment having a charge of -0.58 and a spin density of 0.61.

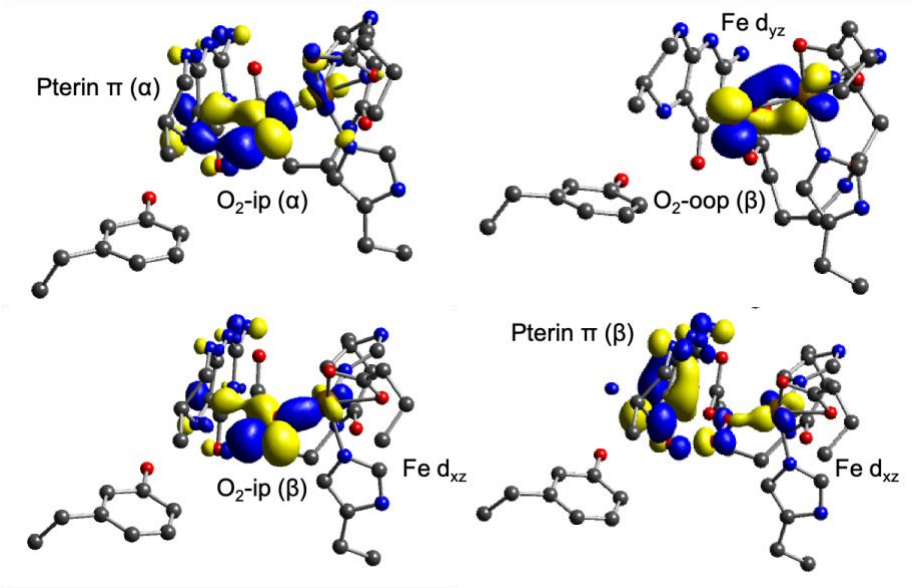

Fig. S35: Occupied contours showing the interactions between the O_2, pterin and Fe fragments. O_2-ip = O_2 in-plane and O_2-oop = O_2 out-of-plane. The bottom two occupied FMOs demonstrate the interaction between the three orbitals (Fe-d_{xz}, O_2-ip and pterin π) that mediate the electron transfer from the pterin to the iron in the carbonyl not bound coordinate.

References

1. Windahl, M. S., Boesen, J., Karlsen, P. E. & Christensen, H. E. M. Expression, Purification and Enzymatic Characterization of the Catalytic Domains of Human Tryptophan Hydroxylase Isoforms. *Protein J.* **28**, 400–406 (2009).
2. Hoops, S. *et al.* COPASI--a COmplex PAthway SImulator. *Bioinformatics* **22**, 3067–3074 (2006).
3. Frisch, M. J. et al. *Gaussian 09, Revision E.01*; Gaussian Inc.: Wallingford CT, 2009.
4. Grimme, S., Antony, J., Ehrlich, S. & Krieg, H. A consistent and accurate ab initio parametrization of density functional dispersion correction (DFT-D) for the 94 elements H-Pu. *J. Chem. Phys.* **132**, 154104 (2010).
5. Weigend, F. & Ahlrichs, R. Balanced basis sets of split valence, triple zeta valence and quadruple zeta valence quality for H to Rn: Design and assessment of accuracy. *Phys. Chem. Chem. Phys.* **7**, 3297 (2005).
6. Cossi, M., Rega, N., Scalmani, G. & Barone, V. Energies, structures, and electronic properties of molecules in solution with the C-PCM solvation model. *J. Comput. Chem.* **24**, 669–681 (2003).
7. Tenderholt, A. L. *QMForge,* Version 2.4, https://qmforge.net.
8. Kieber-Emmons, M. T. *LUMO,* Version 1.0.3, 2014.
9. Gilbert, A. *IQmol,* Version 2.10.0, 2016.
10. Solomon, E. I. *et al.* Geometric and Electronic Structure/Function Correlations in Non-Heme Iron Enzymes. *Chem. Rev.* **100**, 235–349 (2000).
11. Pavel, E. G., Kitajima, N. & Solomon, E. I. Magnetic Circular Dichroism Spectroscopic Studies of Mononuclear Non-Heme Ferrous Model Complexes . Correlation of Excited- and Ground-State Electronic Structure with Geometry. *J. Am. Chem. Soc.* **120**, 3949–3962 (1998).
12. Krzyaniak, M. D., Eser, B. E., Ellis, H. R., Fitzpatrick, P. F. & McCracken, J. Pulsed EPR Study of Amino Acid and Tetrahydropterin Binding in a Tyrosine Hydroxylase Nitric Oxide Complex: Evidence for Substrate Rearrangements in the Formation of the Oxygen-Reactive Complex. *Biochemistry* **52**, 8430–8441 (2013).
13. McCracken, J., Eser, B. E., Mannikko, D., Krzyaniak, M. D. & Fitzpatrick, P. F. HYSCORE Analysis of the Effects of Substrates on Coordination of Water to the Active Site Iron in Tyrosine Hydroxylase. *Biochemistry* **54**, 3759–3771 (2015).
14. Goodwill, K. E., Sabatier, C. & Stevens, R. C. Crystal Structure of Tyrosine Hydroxylase with Bound Cofactor Analogue and Iron at 2.3 Å Resolution: Self-Hydroxylation of Phe300 and the Pterin-Binding Site. *Biochemistry* **37**, 13437–13445 (1998).
15. Goodwill, K. E. *et al.* Crystal structure of tyrosine hydroxylase at 2.3 Å and its implications for inherited neurodegenerative diseases. *Nat. Struct. Biol.* **4**, 578–585 (1997).
16. Chow, M. S. *et al.* Spectroscopy and Kinetics of Wild-Type and Mutant Tyrosine Hydroxylase: Mechanistic Insight into O_2 Activation. *J. Am. Chem. Soc.* **131**, 7685–7698 (2009).
17. Moore, J., Wood, J. M. & Schallreuter, K. U. H_2O_2-mediated oxidation of tetrahydrobiopterin: Fourier transform Raman investigations provide mechanistic implications for the enzymatic utilization and recycling of this essential cofactor. *J. Raman Spectrosc.* **33**, 610–617 (2002).
18. Moran, G. R., Derecskei-Kovacs, A., Hillas, P. J. & Fitzpatrick, P. F. On the Catalytic Mechanism of Tryptophan Hydroxylase. *J. Am. Chem. Soc.* **122**, 4535–4541 (2000).